Effects of plasma sheet properties on storm-time ring current

Yihua Zheng,[1,2] Anthony T. Y. Lui,[1] and Mei-Ching Fok[3]

Received 20 August 2009; revised 26 January 2010; accepted 3 February 2010; published 18 August 2010.

[1] Using an electrically self-consistent kinetic ring current model, we investigate how different conditions of plasma sheet distribution affect the ring current properties. Results include comparative studies in (1) varying the radial distance of the plasma sheet boundary; (2) varying local time distribution of the source population; (3) varying the source spectra, with #2 as our main focus. Our results show that a source that is farther away from Earth leads to a stronger ring current than a source that is closer to the Earth. Local time distribution of the source plays an important role in determining both the radial and azimuthal (local time) location of the ring current peak pressure. We found that postmidnight source locations generally lead to a stronger ring current. This finding is in agreement with Lavraud et al. (2008). However, our results do not exhibit any simple dependence of the local time distribution of the peak ring current (within the lower energy range) on the local time distribution of the source, as suggested by Lavraud et al. (2008). Instead, the local time distribution of source populations has to compete with the dynamically updated self-consistent electric field (through the coupling to the ionosphere) in controlling the ring current intensity and peak location. Our results also show that different source spectra lead to different (though the difference may not be very significant) ring current intensities and that low-energy plasma in the kiloelectron volt range at the boundary constitutes a dominant source population to the ring current. In addition, we found that the radial location of source population is also important to ring current development.

Citation: Zheng, Y., A. T. Y. Lui, and M.-C. Fok (2010), Effects of plasma sheet properties on storm-time ring current, *J. Geophys. Res.*, *115*, A08220, doi:10.1029/2009JA014806.

1. Introduction

[2] Plasma sheet plasmas, as one of the important source populations of the ring current, have been examined quite extensively for their characteristics (such as their solar wind/interplanetary magnetic field dependence, local time distribution, etc.) and their role in ring current development. Observations [e.g., *Thomsen et al.*, 2003; *Lavraud et al.*, 2006] as well as drift-loss kinetic ring current simulations [e.g., *Chen et al.*, 2007] have found that a cold dense plasma sheet leads to an enhanced ring current. In particular, a number of studies [e.g., *Kozyra et al.*, 1998; *Chen et al.*, 2000; *Liemohn et al.*, 2001; *Ebihara et al.*, 2005a] have demonstrated that plasma sheet density is crucial to a strong ring current. The highly variable nature of the plasma sheet parameters has been attributed to the complicated structure of the plasma pressure in the inner magnetosphere and the resulting dynamic behavior of rapid subauroral plasma flows [*Ebihara et al.*, 2009].

[3] The availability of satellite observations has advanced our understanding of plasma sheet plasma properties in response to different solar wind conditions. The plasma sheet is colder and denser during intervals of the northward interplanetary magnetic field (IMF) than those of the southward IMF [e.g., *Terasawa et al.*, 1997; *Wing and Newell*, 2002]. During periods of northward IMF, plasma sheet ions often have two components: a hot population of magnetospheric origin and a cold one of magnetosheath origin; the density of the cold plasma sheet ions is usually higher at the dawn flank than the dusk flank [e.g., *Wing et al.*, 2005; *Wang et al.*, 2007] when the solar wind speed (V_{sw}) is small. Prompted by these observational features, *Lavraud and Jordanova* [2007] and *Chen et al.* [2007] recently investigated how two representative plasma sheet conditions (cold dense versus hot tenuous) affect the evolution of the ring current differently, with the former varying density and temperature with conservation of the pressure and the latter based on the statistical results of Geotail observations [*Wang et al.*, 2007]. The effects of Local Time (LT) asymmetry of plasma sheet properties on proton ring current energy and peak location have also been examined. *Lavraud et al.* [2008] provides important insights concerning how local time distribution of plasma sheet density affects the morphology and strength of the ring current. However, the results were performed under a dipole magnetic field and the Volland-Stern empirical electric field model,

[1]Johns Hopkins University Applied Physics Laboratory, Laurel, Maryland, USA.
[2]Now at Space Weather Laboratory, NASA Goddard Space Flight Center, Greenbelt, Maryland, USA.
[3]NASA Goddard Space Flight Center, Greenbelt, Maryland, USA.

Copyright 2010 by the American Geophysical Union.
0148-0227/10/2009JA014806

which may be too simplistic for representing storm time fields. Past research has shown the magnetic field can have large depressions during the storm periods [e.g., *Le et al.*, 2004; *Zaharia et al.*, 2005; *Sitnov et al.*, 2008]. The presence of a spatially localized enhancement of the large-scale electric field between $L = 3$ and $L = 6$ for $Kp > 3$ observed by the CRRES spacecraft is not consistent with what can be predicated by the Volland-Stern model [*Rowland and Wygant*, 1998]. Therefore, one of the major objectives of the paper is to study the influence of local time asymmetry of the plasma sheet density on the ring current dynamics using the Comprehensive Ring Current Model (CRCM) [*Fok et al.*, 2001], which achieves self-consistency in the electric field. In comparison to the work of *Lavraud et al.* [2008], our results highlight the importance of a self-consistent electric field in determining the intensity and morphology of the ring current pressure. The implication of the results is that besides the local time features of the plasma sheet density, other physical parameters, such as the morphology of the global electric field, which is closely related to the spatial and temporal characteristics of the ionospheric conductance, may play important roles in controlling local time distribution of the ring current. In addition, we examine how variations in the radial distance of plasma sheet source population and its spectrum affect the dynamics of the ring current. This work is particularly significant in view of recent observational features of plasma sheet properties [e.g., *Liemohn et al.*, 2008; *Wang et al.*, 2007; *Zhang et al.*, 2006] and their potential impact on the storm-time ring current.

2. Model Description

[4] The CRCM [*Fok et al.*, 2001] is a simulation code that self-consistently solves the bounce-averaged Boltzmann convection-diffusion equation of ring current particles and the continuity of electric current in the coupled magnetosphere and ionosphere system. As a combination of the Fok et al. ring current model [e.g., *Fok and Moore*, 1997] and Rice Convection Model (RCM) [*Toffoletto et al.*, 2003, and references therein], the CRCM has been successful in modeling the storm-time ring current behavior, as well as the dynamics of the coupled ionosphere [e.g., *Ebihara and Fok*, 2004; *Zheng et al.*, 2006]. Details can be found in *Fok et al.* [2001].

[5] Averaging over gyro-phase and bounce-phase, the ring current particle motion is described by the bounce-averaged Boltzmann equation in space and time [*Fok et al.*, 2001], that is

$$\frac{\partial \bar{f}_s}{\partial t} + \langle \dot{\lambda}_i \rangle \frac{\partial \bar{f}_s}{\partial l_i} + \langle \dot{\varphi}_i \rangle \frac{\partial \bar{f}_s}{\partial \varphi_i} = \left\langle \left(\frac{\delta \bar{f}_s}{\delta t} \right)_{\text{loss}} \right\rangle + \left\langle \left(\frac{\delta \bar{f}_s}{\delta t} \right)_{\text{diff}} \right\rangle, \quad (1)$$

where $\bar{f}_s = \bar{f}_s(\lambda_i, \varphi_i, M, K)$ is the four-dimensional phase space density for a given time and species s, λ_i is the magnetic latitude at ionospheric altitude ($r_i \approx 1.02\ R_E$), φ_i is the magnetic local time at the ionospheric altitude, M and K are two adiabatic invariants. The dimensions/grid sizes are 48 in λ_i, 48 in φ_i, 35 in M (first adiabatic invariant), and 28 in K (second adiabatic invariant). The first term on right-hand side of equation (1) includes losses from charge exchange, Coulomb collisions, and loss-cone loss and the second term represents source/loss due to wave-particle interactions. Only charge exchange and loss cone losses are considered here. The operation $\langle\rangle$ means a bounce average over a field line between two mirror points. The bounce-averaged drift velocity $\langle \dot{\lambda}_i \rangle$ and $\langle \dot{\varphi}_i \rangle$ can be represented as partial derivatives of the Hamiltonian (H) as in the paper by *Fok and Moore* [1997, equation (8)], which are elegant and easy to solve numerically. The loss-cone altitude is set at 120 km. The phase space density specified in the $\lambda_i - \varphi_i - M - K$ space $\bar{f}_s = \bar{f}_s(\lambda_i, \varphi_i, M, K)$ can be easily mapped to the $L - MLT - W - \alpha_o$ space (where L is the magnetic shell; MLT is the magnetic local time; W is the particle kinetic energy; α_o is the equatorial pitch angle) $\bar{f}_s = \bar{f}_s(L, MLT, W, \alpha_o)$ that is convenient for comparison with observations.

[6] The RCM algorithm is used to connect the ring current particles in the magnetosphere to the field-aligned currents in the ionosphere based on conservation of number of particles and the current continuity equation. The phase space density $\bar{f}_s = \bar{f}_s(\lambda_i, \varphi_i, M, K)$ is converted to $\eta(\lambda_i, \varphi_i, M, K)$, which represents the number of particles per unit magnetic flux in the ranges of (M, $M + \Delta M$), (K, $K + \Delta K$). The relation is

$$\eta = 4\sqrt{2}\pi m_0^{3/2} \bar{f} M^{1/2} \Delta M \Delta K. \quad (2)$$

The field-aligned current is then given by

$$\frac{J_{\|i}}{B_i} = \sum_s \frac{B}{B^2} \bullet (\nabla \eta_s \times \nabla W_s), \quad (3)$$

where index i represents quantities evaluated at ionosphere altitude (r_i). Equation (3) is equivalent to the so-called Vasyliunas relation [*Vasyliunas*, 1970, 1984].

[7] The ionospheric Φ_i (therefore the electric field) is obtained by solving the Poisson equation

$$\nabla \bullet (-\Sigma \bullet \nabla \Phi_i) = J_{\|i} \sin I, \quad (4)$$

where Σ is the height-integrated conductance tensor and I is the magnetic dip angle in the ionosphere. The ionospheric conductance Σ includes contributions both from solar irradiance (background) and from the auroral particle precipitation. The International Reference Ionosphere (IRI-95) [*Bilitza*, 1997] and the Mass Spectrometer Incoherent Scatter (MSIS-E90) model are used to calculate the background conductance. The Hardy model is used as a default for calculating the auroral conductance, which is Kp dependent [*Hardy et al.*, 1987].

[8] The ionospheric electric potential Φ_i calculated by equation (4) is mapped along magnetic field lines assuming that the field line is equipotential. The newly updated electric field is then used to solve the kinetic equation for ring current particles (equation (1)).

[9] The CRCM can take any magnetic field model (one of the Tsyganenko models is usually used, such as the one developed by *Tsyganenko and Stern* [1996] or by *Tsyganenko and Sitnov* [2005]) or outputs from an MHD model to specify its magnetic field. The Weimer 2000 model [*Weimer*, 2001] is usually employed to set up the potential distribution at the high-latitude boundary. But the CRCM can take results from any empirical models of the electric field or measurements (such as SuperDARN radar) for its high-latitude potential. The *default* distribution function of the injected

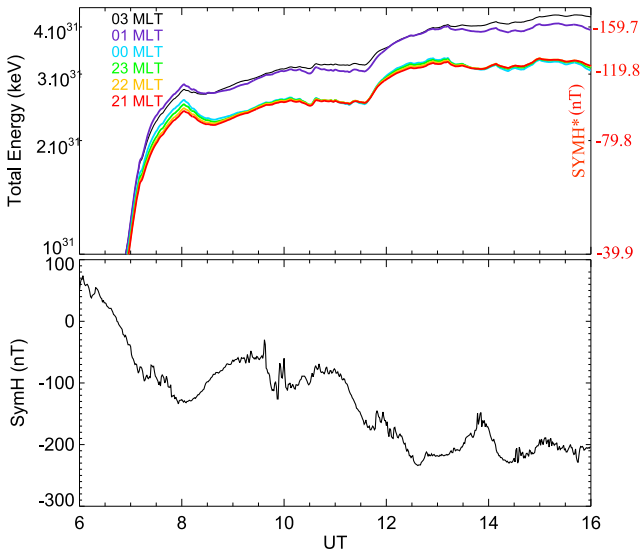

Figure 1. Total energy versus time for six different runs (top), along with the calculated corresponding value of the corrected SymH − SymH*, in reference to the measured SymH index (bottom) during the period of 06–16 UT. The density peak of source population for the six cases is centered at 03 MLT (black), 01 MLT (blue), 00 MLT (light blue), 23 MLT (green), 22 MLT (orange) and 21 MLT (red). A logrithmic scale is used for the top graph and a linear scale is used for the bottom graph.

particles at the boundary (normally it is set at 10 R_E and can be also set at 6.6 R_E to take advantage of the LANL data as in the work of *Ebihara et al.* [2005b]) is assumed to be a Maxwellian with density (n) and temperature (T) linearly dependent on solar wind density and speed, respectively [*Borovsky et al.*, 1998; *Ebihara and Ejiri*, 2000] as described by equations (9) and (10) in *Zheng et al.* [2006]. The CRCM is flexible in adopting any model of plasma sheet source population, such as the recent empirical Tsyganenko and Mukai model [*Tsyganenko and Mukai*, 2003] that is based on the Geotail measurements.

[10] Although our simulation results are the primary concern of this paper, the solar wind and IMF parameters for setting up a proper boundary condition/model input that are required by the CRCM are based on the measurements of the 24 November 2001 event [*Zheng et al.*, 2008]. We focus on the results during the period 0600–1600 UT, which is representative of the main phase of an intense storm (see the bottom graph in Figure 1).

[11] The Weimer 2000 [*Weimer*, 2001] electric field model (parameterized by solar wind conditions) was used to set up the high-latitude boundary condition for the simulation. The input parameters for the Weimer model are derived from the 1 h shifted ACE measurements averaged over 5 min. In order to highlight the effects of source population, the input parameters for the T96 model [*Tsyganenko*, 1995] were kept constant (the set of parameters for 06 UT were used since we started simulation runs at this time: the solar wind dynamic pressure is set as 1.81 nPa, *Dst* as −9.9 nT, IMF By = 6.0 nT and IMF Bz = −1.3 nT). The corotation electric field was also included.

[12] The magnetosphere was assumed to be initially filled with preexisting particles whose distribution function was obtained from measurements of the Active Magnetospheric Particle Tracer Explorers/Charge Composition Explorer satellites during quiet time [*Sheldon and Hamilton*, 1993]. The distribution function of the preexisting particles does not significantly affect the result because the preexisting particles will be subject to loss soon after the enhancement of the convection electric field as the newly injected particles occupy the inner magnetosphere.

3. Simulation Results

3.1. Dependence on Source MLT Distribution

[13] To investigate the effects of the local time distribution of source population density, a variety of numerical experiments were performed. Only protons are considered here in the simulations. Different density profiles were applied at the simulation boundary (10 R_E at the nightside and the magnetopause location determined by the T96 model on the dayside), with a density peak of 1.5 cm^{-3} spanning 4 h in MLT on the nightside and a density of 0.75 cm^{-3} elsewhere. All the other input/boundary conditions, such as the high-latitude potential distribution, were kept the same. The top graph in Figure 1 shows the temporal evolution of the total energy (and the corresponding corrected SymH index: SymH*; the relationship between SymH* and SymH is shown as in equation (5) the paper by *Ebihara et al.* [2005b]) within the simulation domain from six simulation runs, in reference to the SymH index during the period (0600–1600 UT, the main phase of an intense storm) shown in the bottom graph of Figure 1. Please note that a logarithmic scale is used for the total energy, while a linear scale is used for SymH. The difference between the six runs lies only in the center location of the source density peak (other input/boundary conditions were kept same for all runs). The center MLT location of the source density peak for six runs is 03 MLT, 01 MLT, 00 MLT, 23 MLT, 22 MLT, and 21 MLT. Different colors were used to differentiate between the cases (black for the 03 MLT run, blue for the 01 MLT run, light blue for the 00 MLT run, green for he 23 MLT run, orange for the 22 MLT run, and red for the 21 MLT run). A noticeable feature of the results is that during all times of the simulation period, the total energy of a source peaking in postmidnight is appreciably larger than that peaking in the premidnight. On the other hand, the difference in the total energy among the premidnight cases is minute/small. The nice orderly increase in total energy from a premidnight centered source to a postmidnight centered source as demonstrated by *Lavraud et al.* [2008, Figure 3] doesn't always hold true here. For example, at ~0800 UT, the run with the source centered at 01 MLT has larger total energy than the 03 MLT run, and later at ~1430 UT the total energy for the 21 MLT case is larger than the 00 MLT and 23 MLT cases.

[14] A more detailed comparison for four selected cases is provided in Figure 2. Figure 2 shows the results at 12 UT (close to the *Dst* minimum) from four simulation runs (corresponding to the four rows of Figure 2) with the center of the source peak density located at 03 MLT, 00 MLT, 23 MLT, and 21 MLT. The column on the left shows the equatorial potential pattern (without the corotation potential). The partial perpendicular pressure (equivalent to the

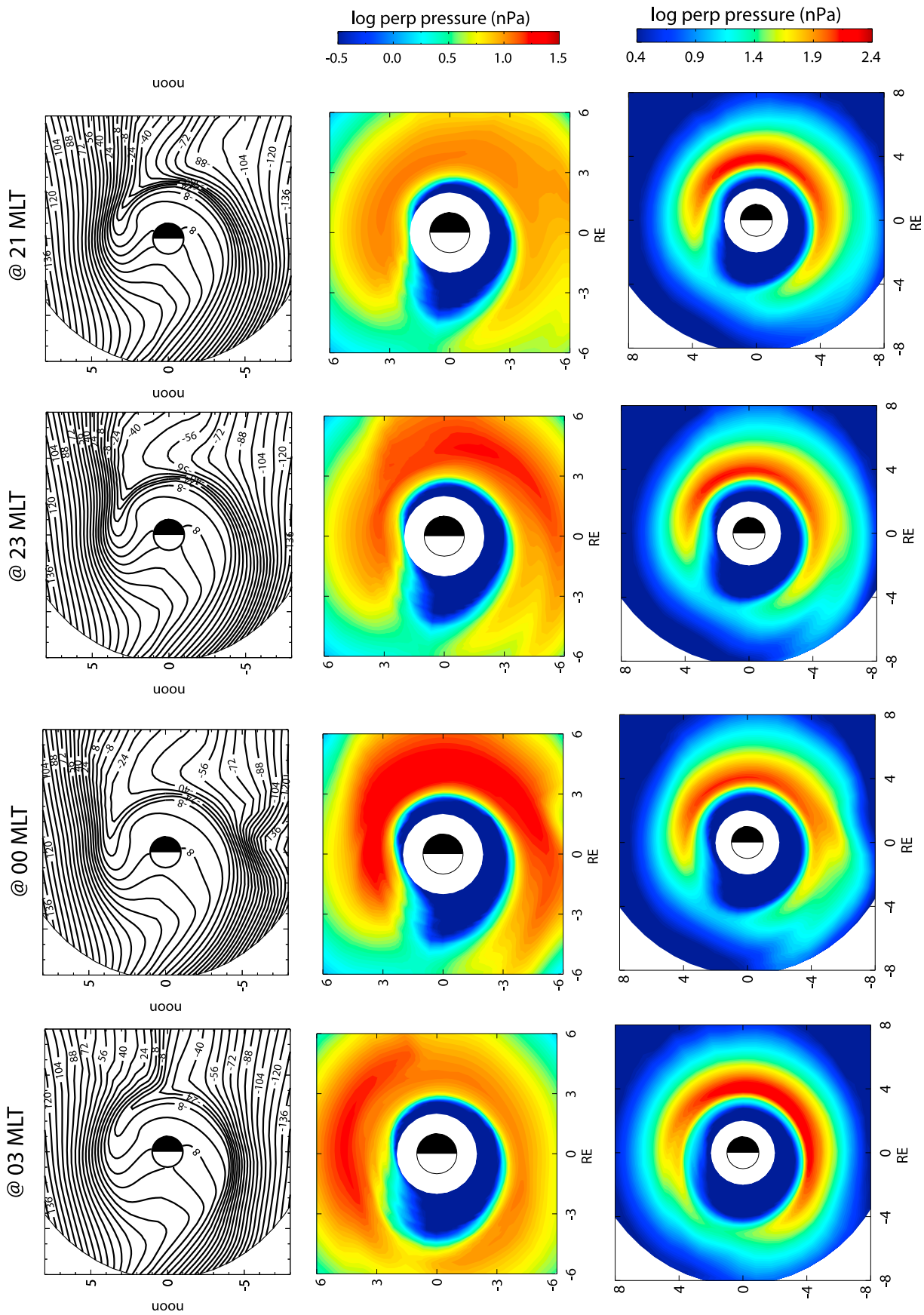
@ 03 MLT
@ 00 MLT
@ 23 MLT
@ 21 MLT
noon
log perp pressure (nPa)
-0.5 0.0 0.5 1.0 1.5
0.4 0.9 1.4 1.9 2.4
RE

Figure 2

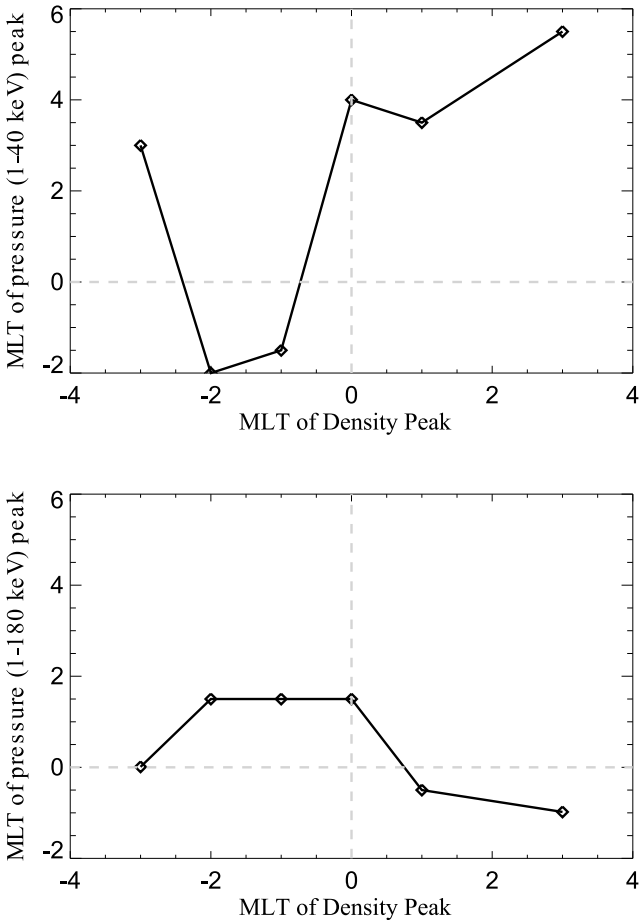

Figure 3. (top) Relationship between the MLT peak of partial pressure in the low energy range of 1–40 keV and the MLT peak of source density. (bottom) Relationship between the MLT peak of the pressure in the range of 1–180 keV and the MLT peak of plasma sheet source.

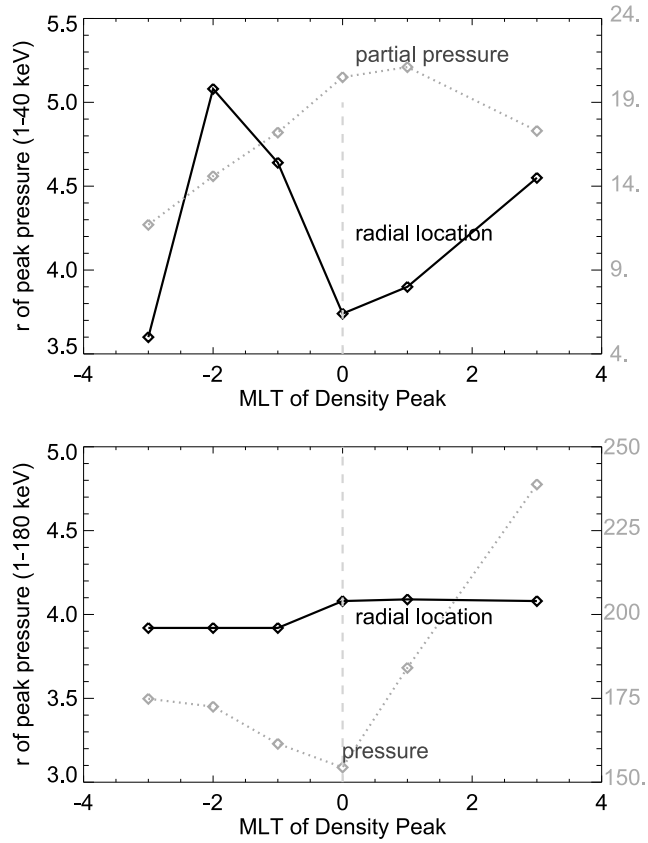

Figure 4. The radial location of the pressure peak versus MLT of the source is shown in black solid line and the peak pressure versus MLT of the source is shown in gray dashed line: (top) partial pressure and (bottom) total pressure.

energy density) in the energy range of 1–40 keV and the perpendicular pressure in the range of 1–180 keV are located in the middle column and on the right, respectively. The electric potential distribution for the four runs (first row), which is important for the low-energy ring current particle motion through $\mathbf{E} \times \mathbf{B}$ drift, shows clear differences between each other, particularly in the 18 MLT-03 MLT sector at the nightside. The partial pressure in the low-energy range displays more noticeable difference between different runs than the pressure in the range of 1–180 keV shown in column on the right. The radial extent of the pressure distribution is larger for the low-energy range.

[15] A quantitative comparison among the six runs in terms of the peak pressure (its MLT value, radial location, and its own value) versus the source MLT distribution is more clearly illustrated in Figures 3 and 4. We recognize that comparisons using the peak pressure alone may be oversimplified. But this method is justified here considering pressure peaks in our results are somewhat broad as indicated by Figures 5 and 6. The magnetically consistent simulation runs of the ring current tend to result in multiple localized peaks in pressure [*Zaharia et al.*, 2005; *Chen et al.*, 2007]. In those circumstances, using the peak pressure alone may be inadequate. The top graph of Figure 3 shows the relationship between the MLT peak of partial pressure in the low-energy range and the MLT peak of the source density. Clearly, the relationship here is very different from what is shown in the paper by *Lavraud et al.* [2008, Figure 4d]. The differences are twofold: (1) the case with its source density peaked at 21 MLT serves as a counterexample in that a premidnight source results in a partial pressure peak in the postmidnight sector (0330 MLT); (2) the MLT location of partial pressure peak and the MLT location of the source exhibit a nonlinear relationship. There is no simple correlation between the source MLT location and the peak pressure MLT location in this low-energy range. As we discuss later, the peak location of the source density only constitutes one of

Figure 2. Simulation results of four runs, with the density peak of the source population centered at 03 MLT, 00 MLT, 23 MLT, and 21 MLT, are shown here. The column on the left is the potential pattern in the corotation frame, the middle column is the partial pressure in the range of 1–40 keV, and the column on the right is the total pressure in the energy range of 1–180 keV. Major features and differences of the four runs are discussed in the text.

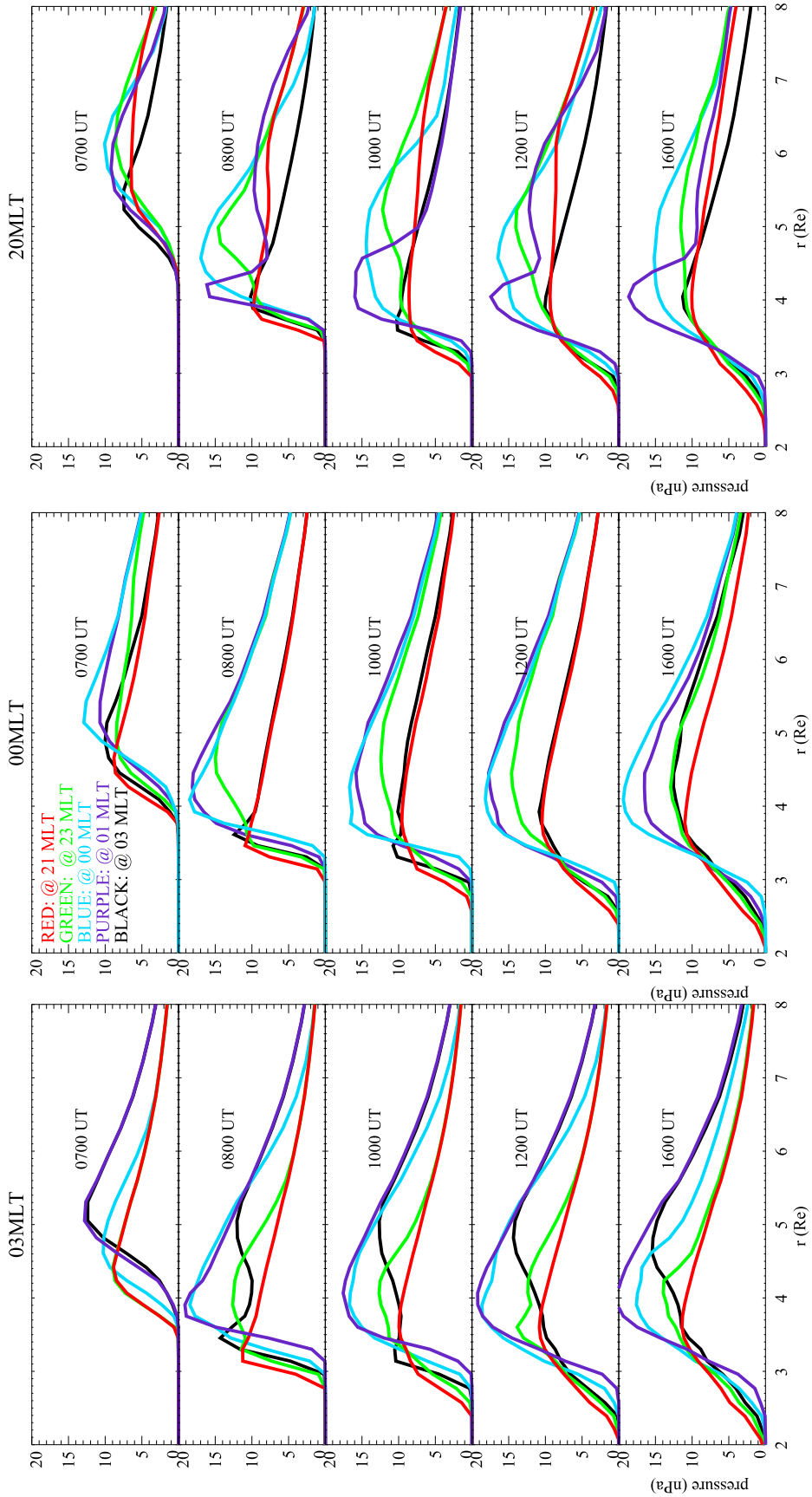

Figure 5. The temporal evolution of the ring current partial pressure versus radial distance at a specific meridional plane for three representative MLTs (03 MLT, 00 MLT, and 20 MLT). The results are from five runs (black line, density peak at 03 MLT; purple line, density peak at 01 MLT; blue line, density peak at 00 MLT; green line, density peak at 23 MLT; red line, density peak at 21 MLT).

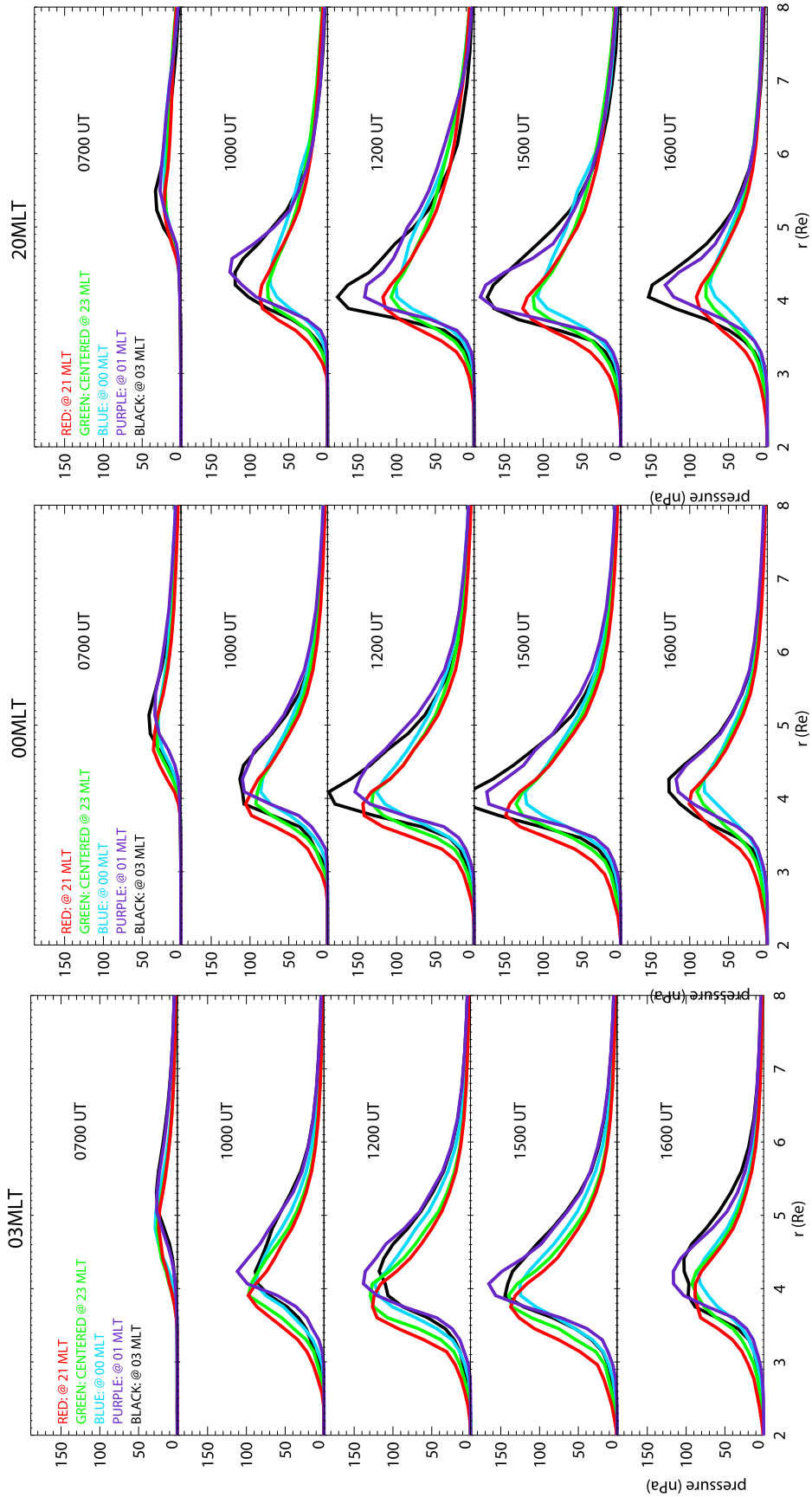

Figure 6. Same format as Figure 5 except that it is for the pressure in the energy range of 1–180 keV.

Table 1. Locations of Peak Pressure Versus MLT Distribution of Source Density

MLT of source density peak	Peak pressure (nPa) (1–40 keV)	r of peak location (R_E)	MLT of peak location	Δr (FWHM)	MLT range	ΔMLT (FWHM)
03 MLT	17.3	4.55	5.5	2.9	1430–0000–0930	19
01 MLT	21.1	3.90	3.5	2.6	1800–0000–0830	14.5
00 MLT	20.5	3.74	4.0	2.1	1900–0000–0830	13.5
23 MLT	17.2	4.64	22.5	3.2	1630–0000–0800	15.5
22 MLT	14.6	5.08	22.0	3.6	1430–0000–0830	18.0
21 MLT	11.7	3.60	3.0	2.8	1730–0000–0830	15.0
Source MLT	**Peak pressure (nPa) (1–180 keV)**	**r of peak location**	**MLT of peak location**	**Δr (FWHM)**	**MLT range**	**ΔMLT (FWHM)**
03 MLT	238.8	4.08	23.0	0.89	1730–0000–0300	9.5
01 MLT	184.1	4.09	23.5	1.11	1730–0000–0500	11.5
00 MLT	154.4	4.08	1.5	1.25	1830–0000–0530	11.0
23 MLT	161.5	3.92	1.5	1.03	1930–0000–0530	10.0
22 MLT	172.5	3.92	1.5	1.18	1830–0000–0500	10.5
21 MLT	174.9	3.92	0.0	1.20	1830–0000–0500	10.5

several factors that controls the peak location of the ring current pressure/energy density.

[16] The bottom graph Figure 3 shows the relationship of the MLT location of peak pressure in the energy of 1–180 keV versus the MLT location of the source density peak. An anticorrelation seems to exist: the postmidnight source leads to a ring current pressure peaking in the premidnight, while a premidnight source leads to a ring current pressure maximizing in the postmidnight (the case where the source density centered at 21 MLT is an exception). The MLT spread of the pressure peak among all the cases is smaller for the total pressure than that of the partial pressure in the 1–40 keV range.

[17] The radial location of the pressure peak (black solid line) and the peak pressure itself (gray dotted line) versus the MLT value of the source density peak are displayed in Figure 4, with the top graph showing the results for the partial pressure and the bottom graph showing those for the total pressure. The span in radial distance among all cases is smaller for the total pressure. The total pressure peak moves closer to the Earth for a premidnight source. From Figure 4 we can see that the pressure arising from ring current particles of 1–40 keV is only a small fraction (less than 10%) of the total pressure (1–180 keV). In addition, the radial location of the partial pressure peak versus MLT of the source does not exhibit the same behavior as shown in the paper by *Lavraud et al.* [2008, Figure 4c]. Neither does the total pressure versus MLT of the source [*Lavraud et al.*, 2008, Figure 4a].

[18] The temporal evolution of the ring current partial pressure (Figure 5) and total pressure (Figure 6) versus radial distance at a specific meridional plane for three representative MLTs (03 MLT, 00 MLT, and 20 MLT) from five runs (density peak at 03 MLT in black, density peak at 01 MLT in purple, density peak at 00 MLT in blue, density peak at 23 MLT in green, and density peak at 21 MLT in red) are shown in Figures 5 and 6, providing a more quantitative view of the differences between the runs. The radial location of the peak pressure is shown more clearly here. The case with the source location centered at 21 MLT has the deepest earthward penetration for both the partial ring current pressure and total pressure. The radial variation of the peak pressure with time is as expected, showing the earthward movement of ring current particles during the early hours of the storm main phase.

[19] The details of the results are summarized in Table 1, where the value of the peak pressure, its radial location, MLT value, full width at half maximum (FWHM) in radial direction, and FWHM in MLT are provided for both the partial pressure and the total pressure.

[20] Differences in the radial and MLT locations among the six cases can be explained by the combination of their electric potential distribution and the MLT distribution of the source population at the boundary. Below we will discuss our results from the comparative analysis between two cases (one with the source density centered at 21 MLT and one with the source density centered at 22 MLT) in order to understand how only a slight difference in the source MLT distribution leads to dramatically different ring current behaviors, particularly for the particles in the low-energy range.

[21] Figure 7 shows the partial perpendicular pressure at 12 UT in the 1–40 keV energy range for two cases. The one centered at 21 MLT (left) has a smaller peak pressure than the one centered at 22 MLT (right). In addition, the MLT location of the peak pressure is different, with the former located in the postmidnight (03 MLT) and the latter in the premidnight (22 MLT). The drift paths of ions at four different times (1000 UT, 1020 UT, 1130 UT, and 1200 UT) are shown in Figure 8, with the 21 MLT case at the top and the 22 MLT case at the bottom. Figure 9 shows the corresponding potential distributions for two cases. The drift paths are for ions with 90° equatorial pitch angle and magnetic moment (M) such that their particle energy is 20 keV at 3.6 R_E, 03 MLT. The drift trajectories are isocontours of the Hamiltonian, H, which is given by *Fok et al.* [2001]:

$$H = W + q\Phi - q\Omega M_E \frac{\cos\lambda_i}{2r_i}, \tag{5}$$

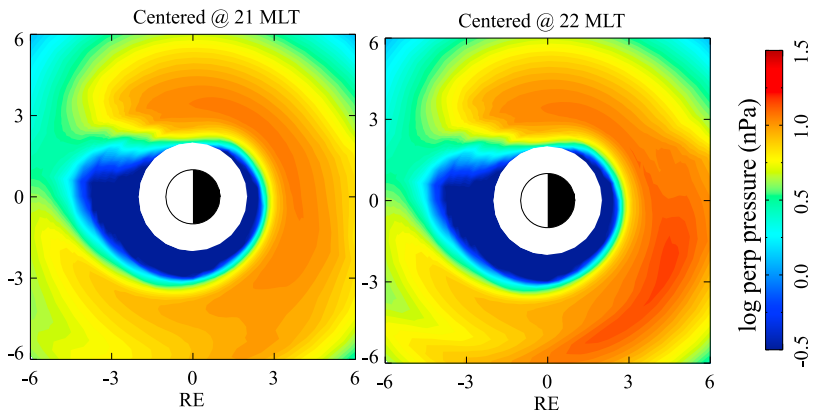

Figure 7. The partial perpendicular pressure in the energy range of 1–40 keV at the equatorial plane for the run with the source density peak centered at 21 MLT and the run centered at 22 MLT.

where W is the ion kinetic energy, which is, for perpendicular particles, equal to $M \bullet B_o$, where B_o is the magnetic field at the equator; Ω is the angular velocity of the Earth's rotation; M_E is the dipole magnetic moment. The dashed lines in Figure 8 are energy contours in kiloelectron volts. The density peak in MLT is marked by the green lines. Besides the differences and similarities in ion drift paths for two cases at any given time, the evolution of ion drift paths with time in response to different potential patterns can be readily seen here. In order to understand the difference occurring at 12 UT, it is necessary to consider the temporal evolution of drift paths/potential patterns prior to the moment of consideration. Notice that the different drift path behavior displayed at 1020 UT might be the major contributor to the differences in partial ring current pressure displayed in Figure 7. For the case with source centered at 21 MLT, a fraction of particles between 19 MLT and 23 MLT at the boundary may have access to the postmidnight sector as indicated by the highlighted path in red. For the case centered at 22 MLT, particles between 20 MLT and

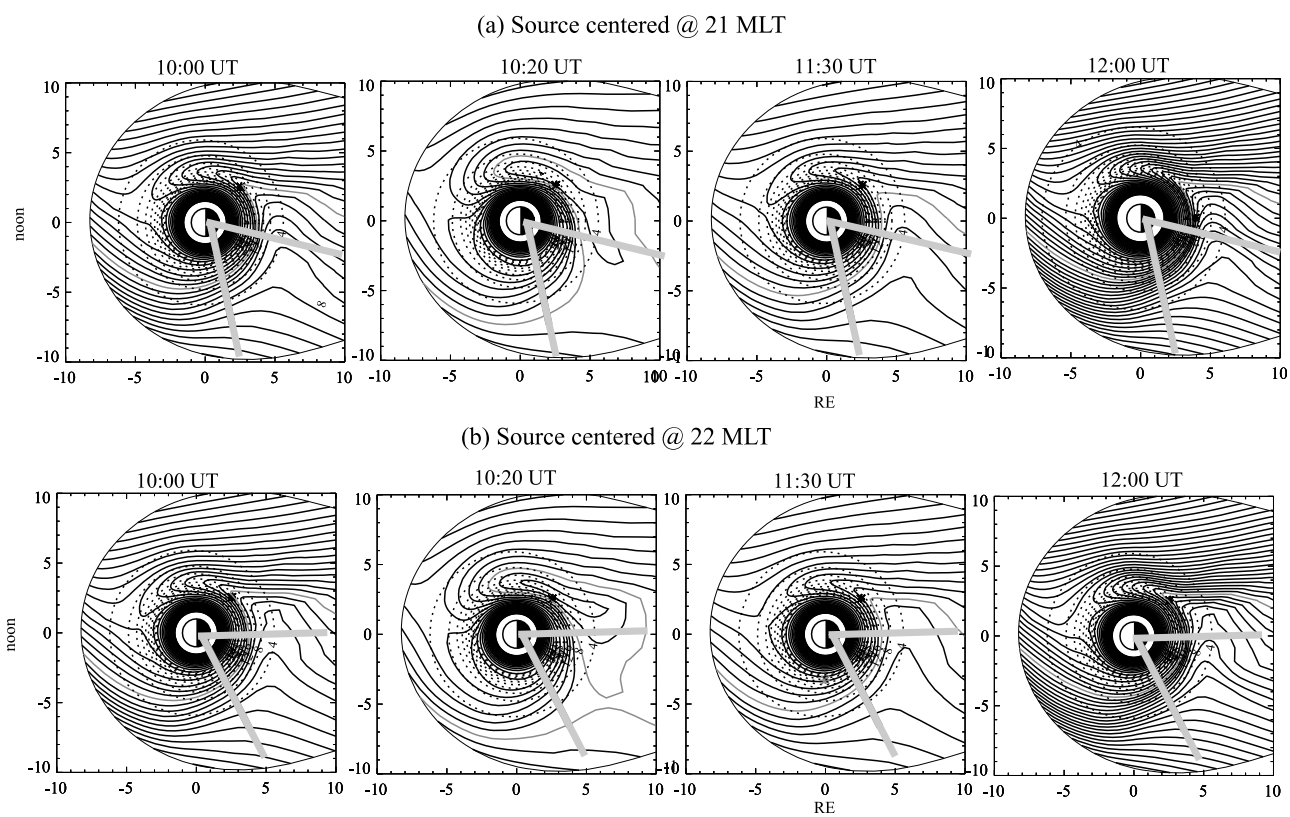

Figure 8. Drift paths at four different times for (a) source centered at 21 MLT and (b) source centered at 22 MLT.

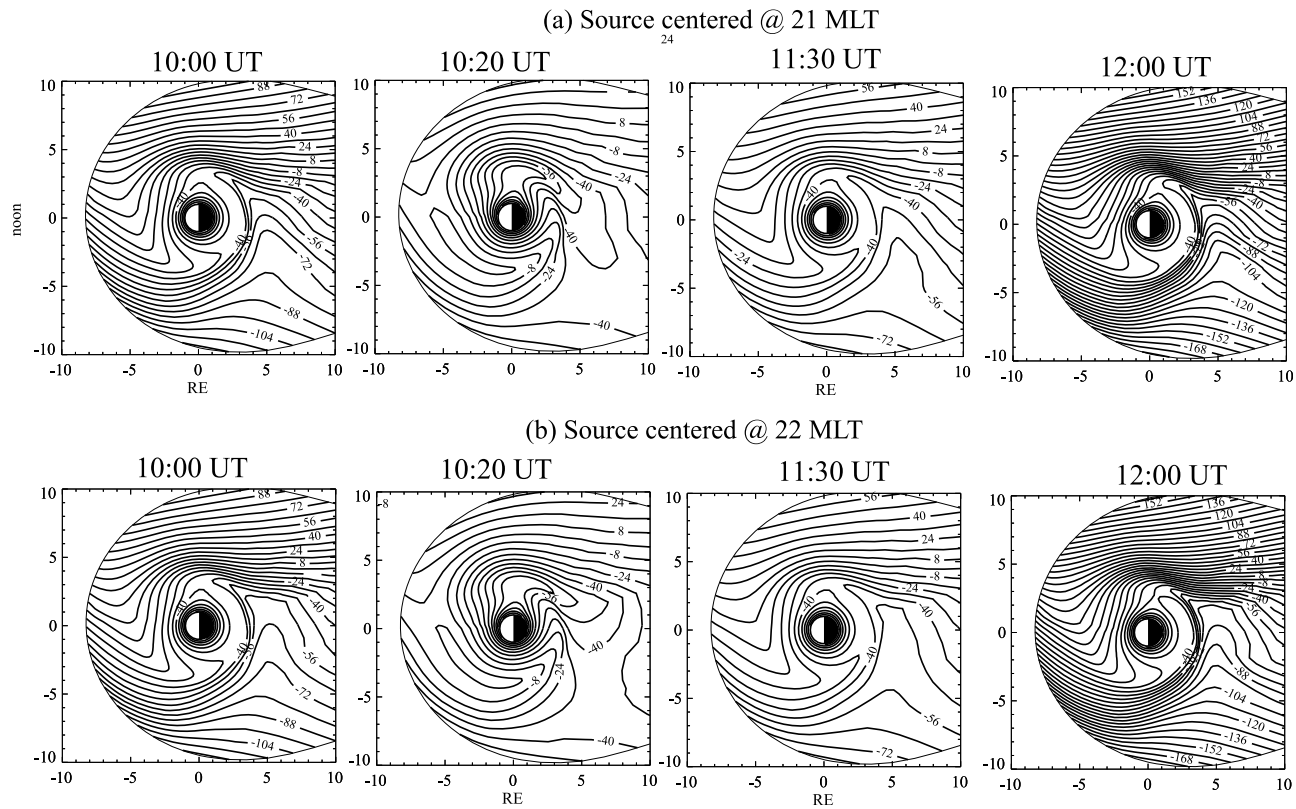

Figure 9. The corresponding potential distributions at four different times for (a) source centered at 21 MLT and (b) source centered at 22 MLT.

24 MLT at the boundary do not seem to have access to the postmidnight sector. Due to modification of the ring current at any time step in the simulation, the self-consistently computed potential distributions in Figure 9 show clear differences between the two cases, particularly at the nightside. The difference in potential distribution leads to the difference in particle trajectory. Therefore, differences in ring current pressure among the six cases can be explained by the combination of their electric potential distribution and the MLT distribution of the source population at the boundary.

3.2. Dependence on Source Radial Location

[22] The appearance of fresh plasma material in the plasma sheet (which serves as one of the major sources for the inner magnetosphere) could come from the episodic events of substorms or aftermaths of interplanetary shocks. Their spatial location will vary depending on the corresponding solar wind and geomagnetic conditions. To examine how the spatial location of plasma sheet plasmas affects the ring current behavior, we show the results of two runs where the distribution of the source is kept the same (assuming Maxwellian, with the same temperature 5 keV and density 0.75 cm^{-3} that are independent of MLT) and the boundary location is set as 10 R_E for run A and 6.6 R_E for run B. Figure 10 shows that a source that is farther away from the Earth produces a much stronger ring current than a source that is closer to the Earth if the distribution of the population is same. This is to be expected, as to the zeroth-order approximation, number of particles in the flux tube is constant so $n*V$ = const (V is magnetic flux tube volume). With the same n assumed for both cases, the number of particles as ring current source population is much smaller at 6.6 R_E than that at 10 R_E. Additionally, betatron and Fermi acceleration should both play a role in ensuring that plasma of equal density and temperature results in a stronger ring current if injected from further away (increase in both perpendicular and parallel energy due to increase in $|\mathbf{B}|$ in the former and decrease in the length of the field line in the latter as plasmas get transported earthward). A more quantitative understanding of how its energy changes as a particle moving earthward is provided in Figure 11 in terms of drift paths for three different pitch angles, with Figure 11a showing the drift paths of particles at ~ 90° equatorial pitch angle, Figure 11b showing the drift paths of particles at ~ 0°, and Figure 11c showing the drift paths for particles at an equatorial pitch angle between 0° and 90°. From the drift paths (solid lines) and the isocontours of energy (dashed lines) in the left column, we can see that particle energy increase as particle moves earthward regardless of its pitch angle. The dashed lines in the right column are isocontours of the sine value of the equatorial pitch angle. Figure 11b indicates that there is an increase in pitch angle as particles convect earthward. At least this is true for the cases under a time-independent magnetic field. Figure 11 also shows that in order for a particle at 10 R_E in the nightside to reach 20 keV at 3.6 R_E, 03 MLT, its

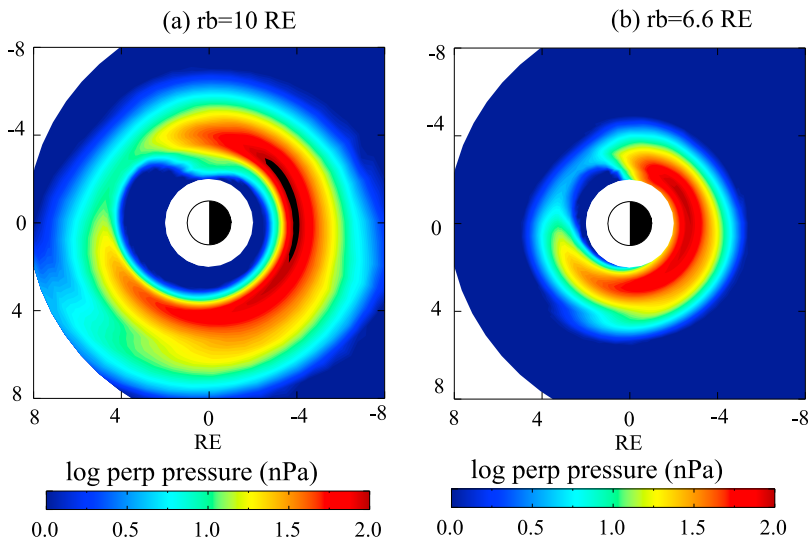

Figure 10. Ring current dependence on source radial distance. The equatorial pressure distribution for (a) source located at 10 R_E and (b) source located at 6.6 R_E.

required energy at the boundary is smallest for particles at 90° pitch angle, largest for particles at 0° pitch angle. In all three cases, particles that are farther away from the source get more energization. The implication of Figure 11 is that pitch angle distribution of the source population is also an important factor in controlling ring current intensity.

[23] This investigation indicates that temporal changes/spatial distribution of the source location could be one of the factors contributing to the structuring of the ring current. The results bear significance to proper modeling and representation of different plasma species, which most likely have very different source locations.

3.3. Dependence on Source Spectrum

[24] To show the dependence of the ring current on the source spectrum, results from two runs are shown in Figure 12, where run 1 assumes a Maxwellian distribution (equation (6)) and run 2 assumes a kappa distribution with $\kappa = 5$ (equation (7)) while keeping same n (0.75 cm^{-3}) and E_o(5 keV) for both cases. The temperature and density are uniform in MLT:

$$f = n\left(\frac{m}{2\pi E_o}\right)^{3/2} \exp^{-\frac{E}{E_o}}, \tag{6}$$

$$f = n\left(\frac{m}{2\pi E_o \kappa}\right)^{3/2} \frac{\Gamma(\kappa+1)}{\Gamma(\kappa-1/2)}\left(1+\frac{E}{E_o}\right)^{-\kappa-1}. \tag{7}$$

Figure 12c shows the density versus energy distribution for both cases with the black line corresponding to the Maxwellian distribution and the red line corresponding to the kappa distribution at the boundary. The equatorial plasma pressure distribution in Figures 12a and 12b shows that with the same density and characteristic energy, the Maxwellian distribution leads to a more enhanced ring current. The total energy versus time from 06 UT to 16 UT shown in Figure 12d also verifies this.

[25] Even though our choice of spectra is relatively simple (the plasma sheet plasma is better represented as a bi-kappa distribution), results from the two runs show that plasma less than 15 keV (the crossover energy in Figure 12c) contribute most to the ring current pressure since the difference between the two distributions lies in these source particles (Figure 12c). To be more general, the important implication of the results is that low-energy plasma in the kiloelectron volt range from the plasma sheet constitutes a dominant source population for the ring current.

4. Discussion and Summary

[26] These results highlight the complexity of the ring current dynamics. The MLT distribution of the source density is an important factor in affecting ring current strength and morphology. But there is no simple linear relationship between the MLT of the source and the MLT value of the peak ring current energy density (pressure) when self-consistency in the electric field is considered. The MLT characteristics of the ring current pressure are determined by multiple factors, with the global electric field distribution as a prominent one. The fundamental equation of ionosphere-magnetosphere coupling [*Vasyliunas*, 1970] is $\vec{\nabla}_i \bullet [\vec{\Sigma} \bullet (-\vec{\nabla}_i \Phi)] = \mathbf{b} \bullet \vec{\nabla}_i V \times \vec{\nabla}_i P \sin(\mathrm{I})$ (where index i refers to the quantities evaluated at the ionosphere, $\vec{\Sigma}$ is the height-integrated conductance tensor, Φ is the electric potential, V is the flux tube volume, P is the ring current pressure, and I is the magnetic dip angle). The ring current strongly affects the electric field in storm times, as *Ridley and Liemohn* [2002] have demonstrated and as indicated by the above equation. To calculate the electric field properly, ring current effects must be taken into account. Conductance inhomogeneity is also important, particularly the day-night effect. Magnetic field configuration is important for ring current particle transport, particularly for the particles at higher energies. Previous modeling results with self-

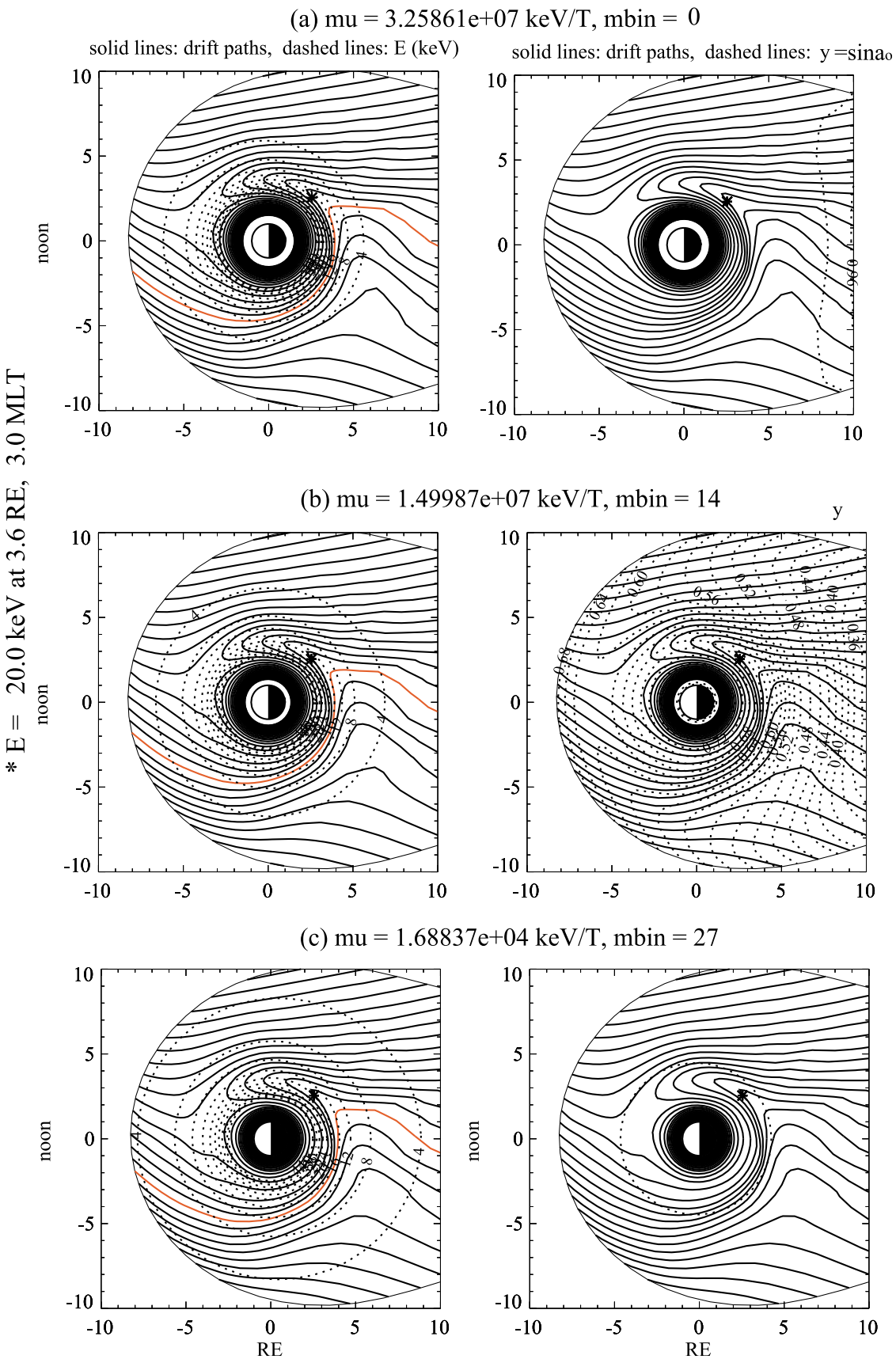

Figure 11. Drift paths for three different equatorial pitch angles, with (a) at ~ 90°, (b) at angle between 0° and 90°, and (c) at ~0°.

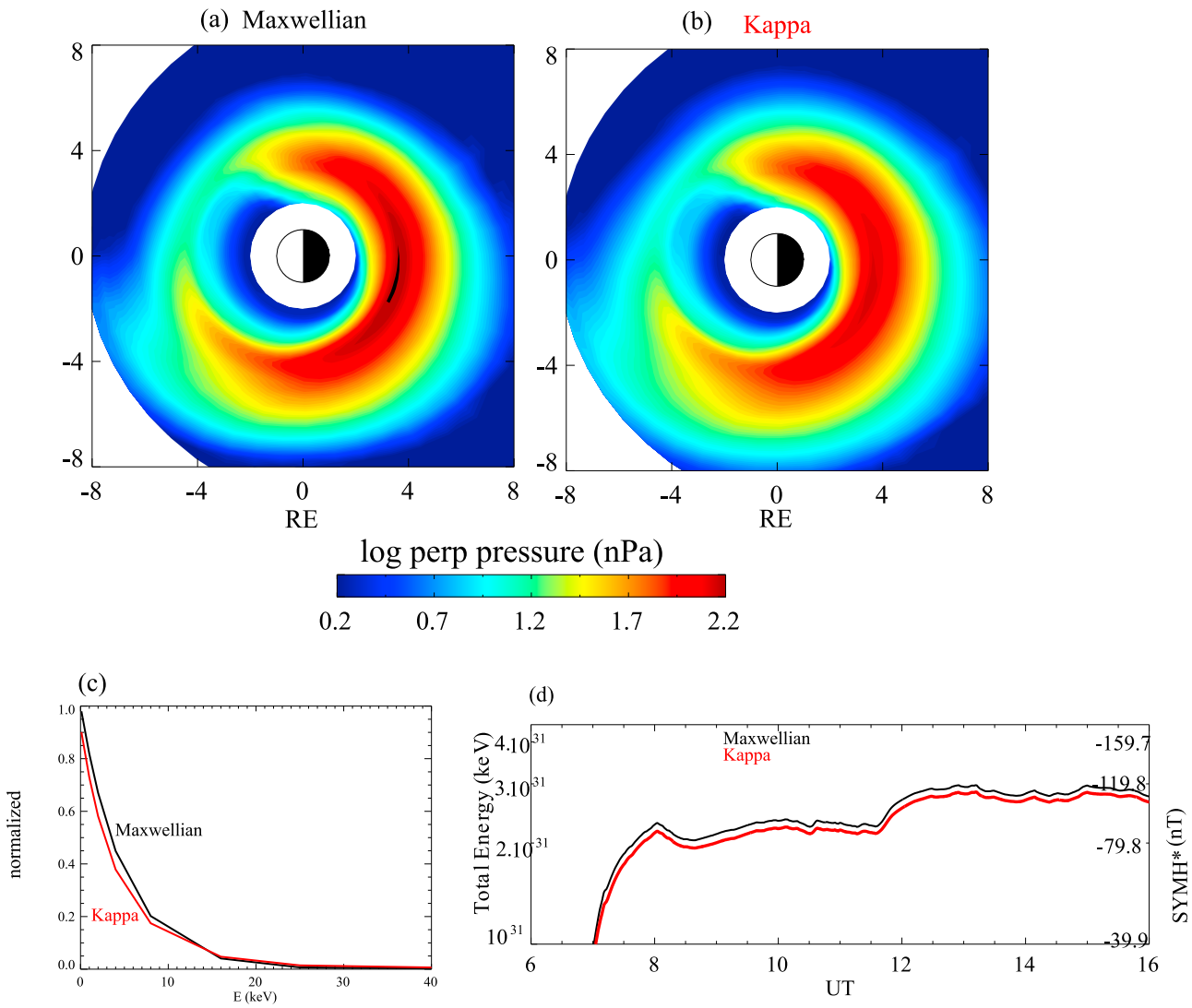

Figure 12. Ring current dependence on the source spectra. Equatorial distribution of the ring current pressure for (a) the case where the source population is represented by a kappa distribution and (b) the case represented by a Maxwellian distribution. (c) Density distribution at the boundary for two cases. (d) Total energy (and the calculated SymH*) versus time during 06 UT–16 UT, in the same format as that in Figure 1.

consistency in **B** show that the total ring current strength decreases in comparison with a dipole field [*Zaharia et al.*, 2006; *Chen et al.*, 2006], and the ring current is more structured. However, the ring current morphology and local time distribution of the equatorial flux peaks remain almost unchanged [*Jordanova et al.*, 2006].

[27] Our numerical experiments also show that the radial location of the source population and their spectra characteristics are important players in dynamic evolution of the ring current. Therefore, the global electric field and ionospheric conductance map, together with the spatial (in radial distance and MLT distribution), temporal, and spectra (plus compositional) makeup of the source population, are all important physical parameters in controlling the ring current morphology and intensity.

[28] In summary, our numerical results show that the source local time location is also a major factor controlling the total ring current energy, with substantially larger total energies obtained for a postmidnight source location (Figure 1) as found in the work of *Lavraud et al.* [2008]. However, one major conclusion of the paper is that self-consistency in the electric field is critical in determining the local time distribution of the ring current pressure. The simple relationship between the peak location of the plasma sheet density and the peak location of the ring current pressure in the low-energy range disappears when the coupling between the ring current and ionosphere is considered. Such results are very different from those generated using the Volland-Stern empirical model. This paper further confirms that a realistic description of the ring current requires a realistic representation (including temporal, spatial, and compositional variations) of the source population at the boundary and the global electric field distribution (which implies the significance of the ionospheric conductance).

[29] **Acknowledgments.** This work was supported by the NASA grants NNX07AG08G, NNX08AM16G and NSF grant 0852508 to JHU/APL. We thank both reviewers for their substantive and constructive comments.

[30] Wolfgang Baumjohann thanks the reviewers for their assistance in evaluating this paper.

References

Bilitza, D. (1997), International reference ionosphere-Status, 1995/96, *Adv. Space Res.*, *20*, 1751.

Chen, M. W., L. R. Lyons, and M. Schulz (2000), Stormtime ring-current formation: A comparison between single-and double-dip model storms with similar transport characteristics, *J. Geophys. Res.*, *105*(A12), 27,755–27,765.

Chen, M. W., S. Liu, M. Schulz, J. L. Roeder, and L. R. Lyons (2006), Magnetically self-consistent ring current simulations during the 19 October 1998 storm, *J. Geophys. Res.*, *111*, A11S15, doi:10.1029/2006JA011620.

Chen, M. W., C.-P. Wang, M. Schulz, and L. R. Lyons (2007), Solar-wind influence on MLT dependence of plasma sheet conditions and their effects on storm time ring current formation, *Geophys. Res. Lett.*, *34*, L14112, doi:10.1029/2007GL030189.

Ebihara, Y., and M. Ejiri (2000), Simulation study on fundamental properties of the storm-time ring current, *J. Geophys. Res.*, *105*(A7), 15,843–15,859.

Ebihara, Y., and M.-C. Fok (2004), Postmidnight storm-time enhancement of tens-of-keV proton flux, *J. Geophys. Res.*, *109*, A12209, doi:10.1029/2004JA010523.

Ebihara, Y., M.-C. Fok, R. A. Wolf, M. F. Thomsen, and T. E. Moore (2005a), Nonlinear impact of plasma sheet density on the storm-time ring current, *J. Geophys. Res.*, *110*, A02208, doi:10.1029/2004JA010435.

Ebihara, Y., M.-C. Fok, S. Sazykin, M. F. Thomsen, M. R. Hairston, D. S. Evans, F. J. Rich, and M. Ejiri (2005b), Ring current and the magnetosphere-ionosphere coupling during the superstorm of 20 November 2003, *J. Geophys. Res.*, *110*, A09S22, doi:10.1029/2004JA010924.

Ebihara, Y., N. Nishitani, T. Kikuchi, T. Ogawa, K. Hosokawa, M.-C. Fok, and M. F. Thomsen (2009), Dynamical property of storm time subauroral rapid flows as a manifestation of complex structures of the plasma pressure in the inner magnetosphere, *J. Geophys. Res.*, *114*, A01306, doi:10.1029/2008JA013614.

Fok, M. C., and T. E. Moore (1997), Ring current modeling in a realistic magnetic field configuration, *Geophys. Res. Lett.*, *24*(14), 1775, doi:10.1029/97GL01255.

Fok, M.-C., R. A. Wolf, R. W. Spiro, and T. E. Moore (2001), Comprehensive computational model of the Earth's ring current, *J. Geophys. Res.*, *106*(A5), 8417, doi:10.1029/2000JA000235.

Hardy, D., A., M. S. Gussenhoven, R. Raistrick, and W. J. McNeil (1987), Statistical and functional representations of the pattern of auroral energy flux, number flux and conductivity, *J. Geophys. Res.*, *92*, 12275, doi:10.1029/JA092iA11p12275.

Jordanova, V. K., Y. S. Miyoshi, S. Zaharia, M. F. Thomsen, G. D. Reeves, D. S. Evans, C. G. Mouikis, and J. F. Fennell (2006), Kinetic simulations of ring current evolution during the Geospace Environment Modeling challenge events, *J. Geophys. Res.*, *111*, A11S10, doi:10.1029/2006JA011644.

Kozyra, J. U., V. K. Jordanova, J. E. Borovsky, M. F. Thomsen, D. J. Knipp, D. S. Evans, D. J. McComas, and T. E. Cayton (1998), Effects of a high-density plasma sheet on ring current development during the November 2–6, 1993, magnetic storm, *J. Geophys. Res.*, *103*(A11), 26,285–26,305.

Lavraud, B., and V. K. Jordanova (2007), Modeling the effects of cold-dense and hot-tenuous plasma sheet on proton ring current energy and peak location, *Geophys. Res. Lett.*, *34*, L02102, doi:10.1029/2006GL027566.

Lavraud, B., M. F. Thomsen, J. E. Borovsky, M. H. Denton, and T. I. Pulkkinen (2006), Magnetosphere preconditioning under northward IMF: Evidence from the study of coronal mass ejection and corotating interaction region geoeffectiveness, *J. Geophys. Res.*, *111*, A09208, doi:10.1029/2005JA011566.

Lavraud, B., V. K. Jordanova, and M. F. Thomsen (2008), Modeling the effects of local time variation of plasma sheet properties on proton ring current energy and peak location, *J. Geophys. Res.*, *113*, A05215, doi:10.1029/2007JA012883.

Le, G., C. T. Russell, and K. Takahashi (2004), Morphology of the ring current derived from magnetic field observations, *Ann. Geophys.*, *22*, 1267–1295.

Liemohn, M. W., J. U. Kozyra, M. F. Thomsen, J. L. Roeder, G. Lu, J. E. Borovsky, and T. E. Cayton (2001), Dominant role of the asymmetric ring current in producing the stormtime *Dst**, *J. Geophys. Res.*, *106*(A6), 10,883–10,904.

Liemohn, M. W., J.-C. Zhang, M. F. Thomsen, J. E. Borovsky, J. U. Kozyra, and R. Ilie (2008), Plasma properties of superstorms at geosynchronous orbit: How different are they?, *Geophys. Res. Lett.*, *35*, L06S06, doi:10.1029/2007GL031717.

Ridley, A. J., and M. W. Liemohn (2002), A model-derived storm time asymmetric ring current driven electric field description, *J. Geophys. Res.*, *107*(A8), 1151, doi:10.1029/2001JA000051.

Rowland, D. E., and J. R. Wygant (1998), Dependence of the large-scale, inner magnetospheric electric field on geomagnetic activity, *J. Geophys. Res.*, *103*(A7), 14,959–14,964.

Sheldon, R. B., and D. C. Hamilton (1993), Ion transport and loss in the Earth's quiet ring current, 1, Data and standard model, *J. Geophys. Res.*, *98*(A8), 13491–13508.

Sitnov, M. I., N. A. Tsyganenko, A. Y. Ukhorskiy, and P. C. Brandt (2008), Dynamical data-based modeling of the storm-time geomagnetic field with enhanced spatial resolution, *J. Geophys. Res.*, *113*, A07218, doi:10.1029/2007JA013003.

Terasawa, T., et al. (1997), Solar wind control of density and temperature in the near-Earth plasma sheet: WIND/GEOTAIL collaboration, *Geophys. Res. Lett.*, *24*(8), 935–938.

Thomsen, M. F., J. E. Borovsky, R. M. Skoug, and C. W. Smith (2003), Delivery of cold, dense plasma sheet material into the near-Earth region, *J. Geophys. Res.*, *108*(A4), 1151, doi:10.1029/2002JA009544.

Toffoletto, F., S. Sazykin, R. Spiro, and R. Wolf (2003), Inner magnetosphere modeling with the Rice Convection Model, *Space. Sci. Rev.*, *107*, 175–196.

Tsyganenko, N. A. (1995), Modeling the Earth's magnetospheric magnetic field confined within a realistic magnetopause, *J. Geophys. Res.*, *100*(A4), 5599–5612.

Tsyganenko, N. A., and T. Mukai (2003), Tail plasma sheet models derived from Geotail particle data, *J. Geophys. Res.*, *108*(A3), 1136, doi:10.1029/2002JA009707.

Tsyganenko, N. A., and I. M. Sitnov (2005), Modeling the dynamics of the inner magnetosphere during strong geomagnetic storms, *J. Geophys. Res.*, *110*, A03208, doi:10.1029/2004JA010798.

Tsyganenko, N. A., and D. P. Stern (1996), Modeling the global magnetic field of the large-scale Birkeland current systems, *J. Geophys. Res.*, *101*(A12), 27187.

Vasyliunas, V. M. (1970), Mathematical models of magnetospheric convection and its coupling to the ionosphere, in *Particles and Fields in the Magnetosphere*, edited by B. M. McCormac, p. 60, D. Reidel, Norwell, MA.

Vasyliunas, V. M. (1984), Fundamentals of current description, in *Magnetospheric Currents*, edited by T. A. Potemra, p. 63, AGU, Washington, D. C.

Wang, C.-P., L. R. Lyons, T. Nagai, J. M. Weygand, and R. W. McEntire (2007), Sources, transport, and distributions of plasma sheet ions and electrons and dependences on interplanetary parameters under northward interplanetary magnetic field, *J. Geophys. Res.*, *112*, A10224, doi:10.1029/2007JA012522.

Weimer, D. R. (2001), An improved model of ionospheric electric potentials including substorm perturbations and application to the Geospace Environment Modeling November 24, 1996, event, *J. Geophys. Res.*, *106*(A1), 407, doi:10.1029/2000JA000604.

Wing, S., and P. T. Newell (2002), 2D plasma sheet ion density and temperature profiles for northward and southward IMF, *Geophys. Res. Lett.*, *29*(9), 1307, doi:10.1029/2001GL013950.

Wing, S., J. R. Johnson, P. T. Newell, and C.-I. Meng (2005), Dawn-dusk asymmetries, ion spectra, and sources in the northward interplanetary magnetic field plasma sheet, *J. Geophys. Res.*, *110*, A08205, doi:10.1029/2005JA011086.

Zaharia, S., M. F. Thomsen, J. Birn, M. H. Denton, V. K. Jordanova, and C. Z. Cheng (2005), Effect of storm-time plasma pressure on the magnetic field in the inner magnetosphere, *Geophys. Res. Lett.*, *32*, L03102, doi:10.1029/2004GL021491.

Zaharia, S., V. K. Jordanova, M. F. Thomsen, and G. D. Reeves (2006), Self-consistent modeling of magnetic fields and plasmas in the inner magnetosphere: Application to a geomagnetic storm, *J. Geophys. Res.*, *111*, A11S14, doi:10.1029/2006JA011619.

Zhang, J., M. W. Liemohn, J. U. Kozyra, M. F. Thomsen, H. A. Elliott, and J. M. Weygand (2006), A statistical comparison of solar wind sources of moderate and intense geomagnetic storms at solar minimum and maximum, *J. Geophys. Res.*, *111*, A01104, doi:10.1029/2005JA011065.

Zheng, Y., A. T. Y. Lui, M.-C. Fok, B. J. Anderson, P. C. Brandt, T. J. Immel, and D. G. Mitchell (2006), Relationship between region 2 field-aligned current and the ring current: Model results, *J. Geophys. Res.*, *111*, A11S06, doi:10.1029/2006JA011603.

Zheng, Y., A. T. Y. Lui, and M.-C. Fok (2008), Viewing perspective in energetic neutral atom intensity, *J. Geophys. Res.*, *113*, A09217, doi:10.1029/2008JA013070.

M.-C. Fok, NASA Goddard Space Flight Center, Code 673, Greenbelt, MD 20771, USA. (mei-ching.h.fok@nasa.gov)

A. T. Y. Lui, Johns Hopkins University Applied Physics Laboratory, 11100 Johns Hopkins Rd., Laurel, MD 20723-6099, USA. (Tony.lui@jhuapl.edu)

Y. Zheng, Space Weather Laboratory, NASA Goddard Space Flight Center, Code 674, Greenbelt, MD 20771, USA. (Yihua.Zheng@nasa.gov)